



# Accelerating fishes increase propulsive efficiency by modulating vortex ring geometry

Otar Akanyeti<sup>a,b,1</sup>, Joy Putney<sup>a,c</sup>, Yuzo R. Yanagitsuru<sup>a</sup>, George V. Lauder<sup>d</sup>, William J. Stewart<sup>a,e</sup>, and James C. Liao<sup>a,1</sup>

<sup>a</sup>The Whitney Laboratory for Marine Bioscience, Department of Biology, University of Florida, St. Augustine, FL 32080; <sup>b</sup>The Department of Computer Science, Aberystwyth University, Ceredigion SY23 3FL, Wales; <sup>c</sup>The School of Biological Sciences, Georgia Institute of Technology, Atlanta, GA 30332; <sup>d</sup>The Department of Organismic and Evolutionary Biology, Harvard University, Cambridge, MA 02138; and <sup>e</sup>The Department of Science, Eastern Florida State College, Melbourne, FL 32935

Edited by David W. Russell, University of Texas Southwestern Medical Center, Dallas, TX, and approved November 13, 2017 (received for review April 10, 2017)

**Swimming animals need to generate propulsive force to overcome drag, regardless of whether they swim steadily or accelerate forward. While locomotion strategies for steady swimming are well characterized, far less is known about acceleration. Animals exhibit many different ways to swim steadily, but we show here that this behavioral diversity collapses into a single swimming pattern during acceleration regardless of the body size, morphology, and ecology of the animal. We draw on the fields of biomechanics, fluid dynamics, and robotics to demonstrate that there is a fundamental difference between steady swimming and forward acceleration. We provide empirical evidence that the tail of accelerating fishes can increase propulsive efficiency by enhancing thrust through the alteration of vortex ring geometry. Our study provides insight into how propulsion can be altered without increasing vortex ring size and represents a fundamental departure from our current understanding of the hydrodynamic mechanisms of acceleration. Our findings reveal a unifying hydrodynamic principle that is likely conserved in all aquatic, undulatory vertebrates.**

acceleration | undulatory swimming | vortex ring | fish | hydrodynamics

Over the course of evolutionary time, patterns of animal locomotion have diversified to take advantage of the physical environment through the interplay of morphology, physiology, and neural control. However, two fundamental principles of locomotion in most animals remain the same: (i) Force is generated by transferring momentum to the environment through repetitive motions such as body undulations and oscillating appendages (legs, fins, or wings), and (ii) the locomotor speed is modulated by controlling the amplitude and frequency of these periodic motions (1, 2). Previous studies have demonstrated that the degrees of freedom in amplitude and frequency control are not limitless, but rather constrained by the physical laws imposed by the environment. For example, flying animals must maintain a high wing-beat frequency to generate enough lift, controlling speed primarily by altering the wing's angle of attack (3). In contrast, the morphology and locomotion strategies of aquatic animals have adapted to moving through a viscous environment where gravitational forces are negligible. Among these strategies, the ancestral state of aquatic locomotion is axial undulation, where muscle contractions bend the body into a mechanical wave that passes from head to tail (4). The interaction of angled body surfaces with the surrounding fluid propels the animal forward, and the movements of the entire body contribute to the overall swimming performance (5–10).

Over the past several decades, a number of studies have investigated the kinematics (11–14), muscle activity (15–18), and hydrodynamics (19–21) of tail movements, in particular how tail-beat amplitude and frequency are controlled during steady swimming. Most undulatory vertebrates such as fishes, alligators, dolphins, and manatees control speed by primarily modulating tail-beat frequency while maintaining a relatively low tail-beat amplitude (22–25). At high steady swimming speeds, tail-beat

amplitude reaches a plateau at around 0.2 body length ( $L$ ). Computational studies (26–29) and experiments with hydrofoils (30, 31) suggest that swimming animals operate in this range to maintain high swimming efficiency.

How do these mechanisms apply when a steadily swimming animal accelerates forward, which is often used to catch prey, avoid predators, or save energy during migrations (32, 33)? One hypothesis is that speed is gained only by further increasing the tail-beat frequency (34–37). Alternatively, an animal can bend its body maximally to accelerate large amounts of fluid, as seen in Mauthner initiated C-starts (38–41). However, emerging studies suggest that forward acceleration exhibits distinct kinematics (42–46) that defy both hypotheses, indicating that acceleration may have its own optimization strategy. Although forward acceleration has been a topic of interest for decades in the field of aquatic locomotion (39, 43), a comprehensive understanding of its prevalence and underlying mechanisms has remained elusive. Here, we identify an undulatory locomotion strategy for forward acceleration by integrating complementary approaches: biological experiments with live fishes and physical experiments with biomimetic fish models.

## Results and Discussion

**Acceleration Kinematics Across Fish Phylogeny.** We discovered that in fishes tail-beat amplitude is consistently higher during acceleration than during steady swimming (Fig. 1). This pattern is conserved across 51 species examined, with representatives from a wide range of phylogenetic positions from chondrichthyes (e.g., bonnethead shark, *Sphyrna tiburo*) to tetraodontiformes (e.g., striped burrfish, *Chilomycterus schoepfi*). These species exhibit vastly different body shapes, ecological habitats, and swimming

### Significance

The ability to move is one of the key evolutionary events that led to the complexity of vertebrate life. The most speciose group of vertebrates, fishes, displays an enormous variation of movement patterns during steady swimming. We discovered that this behavioral diversity collapses into one movement pattern when fishes are challenged to increase their swimming speed, regardless of their body size, shape, and ecology. Using flow visualization and biomimetic models, we provide the first mechanistic understanding of how this conserved movement pattern allows fishes to accelerate quickly.

Author contributions: O.A. and J.C.L. designed research; G.V.L. provided the setup for robotic experiments; O.A., J.P., Y.R.Y., G.V.L., and J.C.L. performed research; O.A. and W.J.S. analyzed data; and O.A. and J.C.L. wrote the paper.

The authors declare no conflict of interest.

This article is a PNAS Direct Submission.

Published under the PNAS license.

<sup>1</sup>To whom correspondence may be addressed. Email: jliao@whitney.ufl.edu or ota1@aber.ac.uk.

This article contains supporting information online at [www.pnas.org/lookup/suppl/doi:10.1073/pnas.1705968115/-DCSupplemental](http://www.pnas.org/lookup/suppl/doi:10.1073/pnas.1705968115/-DCSupplemental).

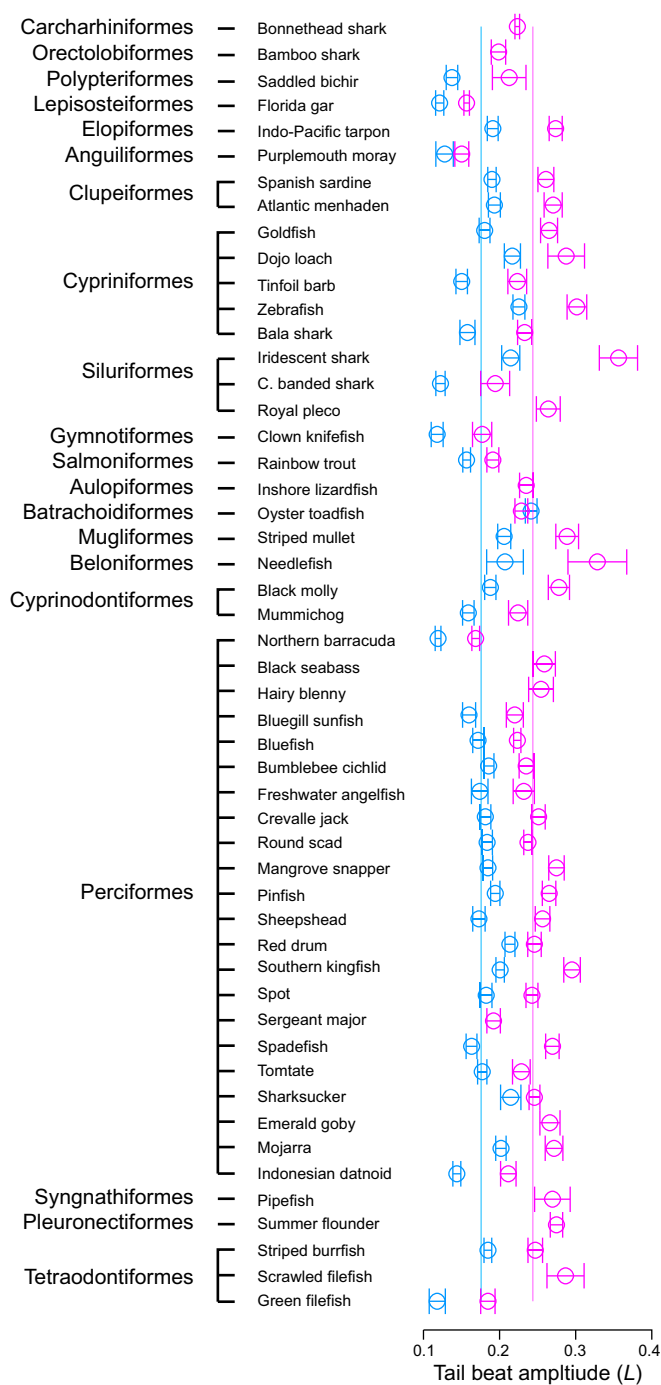


**Fig. 1.** Fishes have higher tail-beat amplitude during acceleration. This phenomenon was confirmed across a wide range of fishes from 20 taxonomic orders with different body shapes, swimming modes, and ecologies. Blue and magenta lines indicate the mean tail-beat amplitudes for steady swimming ( $0.181 \pm 0.004 L$ ) and acceleration ( $0.244 \pm 0.006 L$ ), respectively. Mean tail-beat amplitudes for steady swimming and acceleration are statistically different (unpaired  $t$  test,  $P < 0.001$ ). During steady swimming, it was not possible to measure the tail-beat amplitude of a few species (black seabass, sergeant major, pipefish, summer flounder, and filefish), as they use primarily median or pectoral fins for propulsion. Error bars are  $\pm 1$  SEM.

modes (Table S1). Some species use median or pectoral fins during steady swimming (e.g., clown knifefish, *Chitala ornata* and sergeant major, *Abudefduf saxatilis*), but always revert to body undulation when they accelerate forward from steady swimming.

When we plotted tail-beat amplitude during acceleration against steady swimming for all species, we found that the relationship is linear (Fig. S1A). This suggests that the relative increase in tail-beat amplitude during acceleration is constant at  $34 \pm 4\%$ . However, there is substantial variation in the absolute amplitude values that depends on body length and shape. For example, when body length is held constant, elongate fishes such as Florida gar (*Lepisosteus platyrhincus*) and Northern barracuda (*Sphyrna borealis*) accelerate with lower tail-beat amplitudes ( $0.19 \pm 0.01 L$ ) compared with more fusiform fishes such as tarpon and red drum ( $0.24 \pm 0.01 L$ ). We also found that during acceleration tail-beat amplitude decreases with body length (Fig. S1B).

To better understand whether there is a common propulsive strategy across fish diversity, we next performed a more detailed midline analysis of the entire body during steady swimming and forward acceleration for 9 species. Despite extreme differences in body shape and swimming mode, we found that all fishes share similar midline acceleration kinematics. These acceleration bouts are usually brief, typically less than five tail beats. All points along the body show higher amplitudes compared with steady swimming, but not as high as seen during C-starts (39, 40) (Figs. S2–S4). Further analyses on the traveling body wave and tail movement suggest efficient force production during acceleration (Table S2). The average values across 10 species for slip ratio, Strouhal number ( $St$ ), and maximum angle of attack ( $\alpha_{max}$ ) are  $0.80 \pm 0.02$ ,  $0.41 \pm 0.01$ , and  $22.71 \pm 0.65^\circ$ , respectively. Slip ratios approaching one reveal high swimming efficiency, while experiments with thrust-producing, harmonically oscillating foils show that propulsive efficiency is maximized when  $St$  falls within the range between 0.2 and 0.5 and  $\alpha_{max}$  is between  $15^\circ$  and  $25^\circ$  (30).

In addition to the species studied here, similar acceleration kinematics were previously observed in American eels (44). These elevated amplitudes are most notable around the head and tail. The onset of acceleration (which can be easily recognized because of strong head yaw and a faster tail beat) provides a reference point to interpret the phase relationship between head and tail. By doing so, we found that the motion of the head always precedes the motion of the tail, indicating that the body wave is initiated by strong head movements in all species, although the timing between head and tail movements is not constant. To more closely investigate the kinematics and hydrodynamics of acceleration, we chose a generalized teleost fish, the rainbow trout (*Oncorhynchus mykiss*). The swimming kinematics of this species have been studied in great detail for steady swimming and other behaviors but not for acceleration (5, 13, 47–54). Like those in other species tested in this study, the body amplitudes of trout are higher during acceleration than during steady swimming (Fig. S5A), and head movements precede the motion of the tail (Fig. S5B).

We next examined how swimming speed and acceleration depend on tail-beat amplitude, given that a range of amplitudes is evident for each behavior (Fig. S5C). As others have shown previously (44), we found that in general tail-beat frequency, not tail-beat amplitude, has the most effect during both behaviors (Fig. S5D). Multiple-regression analysis revealed that steady swimming speed increases only with tail-beat frequency. This trend is similar during acceleration, although tail-beat amplitude also has a minor effect (Table S3). Our results suggest that tail-beat amplitude does not change during steady swimming or acceleration, but jumps discretely by  $\sim 30\%$  when fish transition from one behavior to another. Thus, trout appear to have two undulatory gears based on tail-beat amplitude, one for steady swimming and another for acceleration. Our results suggest that this discrete jump in tail-beat amplitude during acceleration is correlated with increased head yaw (Fig. S5E), and these movements are tightly phase locked, with the head preceding the tail (Fig. S5F).

**Hydrodynamic Effects of Increased Tail-Beat Amplitude During Acceleration.** We next investigated how increased tail-beat amplitude relates to thrust production and propulsive efficiency by

using a combination of quantitative flow visualization experiments on live fish and experiments with actuated, soft-bodied robotic models. Results from particle image velocimetry show that fish can reach a maximum acceleration rate of  $20 L \cdot s^{-2}$  from initial swimming speed of  $3 L \cdot s^{-1}$ . To accomplish this, fish transfer more axial momentum to the fluid by generating stronger vortices compared with steadily swimming fish (Fig. 2A). Similar wake structures were previously observed in zebrafish (55), eel (44), and carp (45). In addition, fish entrain more fluid around their posterior body to strengthen shed vortices (Fig. 2B). This occurs because the posterior body has a greater curvature, which creates a low-pressure region in the concavity (Fig. 2B,  $t = 12.5$  ms). The entrained fluid in this low-pressure region (blue) follows the traveling body wave until it reaches the trailing edge of the tail ( $t = 50$  ms). At the point when the tail reverses direction, the fluid starts to roll off the tail and into the

wake ( $t = 56.3$  ms). Concurrently, the body concavity causes flow to build up on the opposite side. This fluid (red) starts getting released to the wake as the tail increases its velocity ( $t = 68.8$  ms). When the tail reaches its maximum velocity, a vortex is formed ( $t = 81.3$  ms), owing to the occurrence of two bodies of fluid moving in opposite directions. Our results indicate that during acceleration body undulations of trout are responsible for increased wake velocity and vorticity. This is not surprising as multiple studies have shown that body-induced flows can enhance vortex shedding in other species (7, 8, 10, 19, 56, 57).

When fish swim, they generate vortex rings (58–60). We see this in two dimensions as two counterrotating vortices (i.e., vortex cores) in the wake after each tail beat (61–63). In recent years, estimating locomotive forces from wake measurements has garnered much interest with hopes of better understanding the resultant motion of the animal (41, 56, 64–66). Several

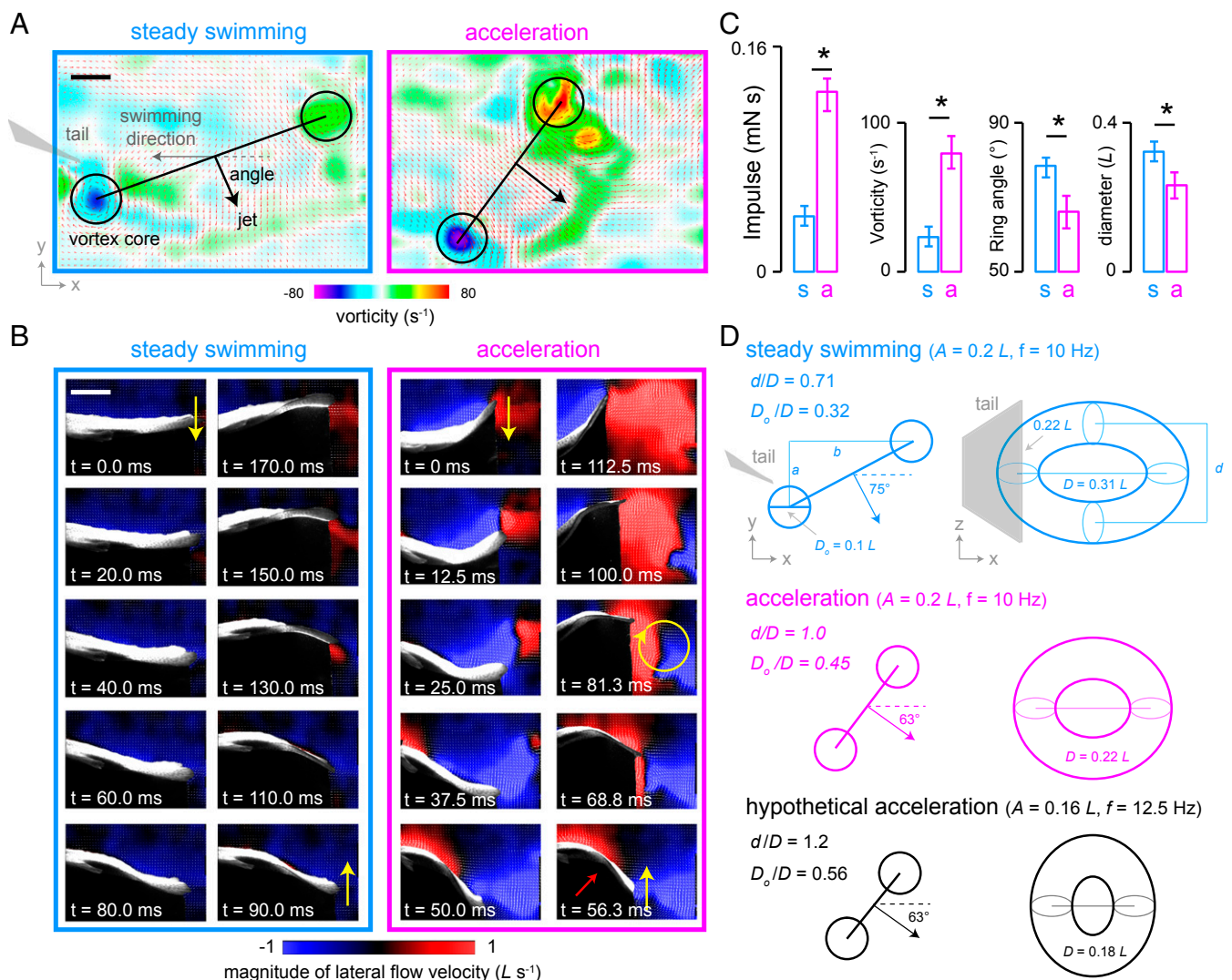


**Fig. 2.** Hydrodynamics of steady swimming vs. acceleration. (A) Representative flow fields behind a rainbow trout ( $L = 32$  cm) swimming steadily at  $3 L \cdot s^{-1}$  (Left) and accelerating (Right) from the same initial speed. The heat map denotes vorticity where negative (magenta) and positive (red) values indicate clockwise and counterclockwise rotation, respectively. (Scale bar, 2 cm.) (B) Body movements of the same fish during steady swimming (Left column) and acceleration (Right column) over one representative tail-beat cycle. Yellow arrows indicate the direction of tail movement. Blue and red denote the magnitude of left and right flow fields, respectively, in the fish frame of reference. In each movie frame, the body of the trout is visible from the dorsal fin to the tail, which represents 30% of the total length. (Scale bar, 4.5 cm.) (C) Mean impulse, vorticity, angle, and diameter of an average vortex ring for steady swimming and acceleration (10 tail beats from each fish,  $n = 2$  fish). \*Significant at  $P < 0.01$ , unpaired  $t$  test. Error bars are  $\pm 1$  SE. (D) Hypothesized vortex ring geometry and orientation behind fish swimming steadily (blue) and accelerating (magenta). Hypothetical acceleration with lower tail-beat amplitude is also shown for comparison (black).



methods have been proposed to estimate locomotive forces (56, 64, 67, 68). The one which we used in this study is based on the classical vortex ring theory (69). We calculated the impulse (i.e., the average force) applied to the fluid during each tail beat by measuring the circulation, jet angle ( $\theta$ ), core diameter ( $D_o$ ), and the spacing between the two vortex cores ( $D$ ). We found that an accelerating trout generates an impulse (along the swimming direction) that is at least four times higher than that required for its initial steady swimming speed (Fig. 2C). This higher impulse is due to a  $172 \pm 16\%$  increase in vorticity. In addition, the jet angle is oriented  $\sim 30 \pm 3\%$  more downstream, which devotes a greater proportion of the impulse along the swimming direction.

We found that  $D$  is reduced by  $\sim 25\%$  from  $0.33 L$  to  $0.25 L$  when fish transition from steady swimming to acceleration. At first glance this may be surprising given that the impulse and kinetic energy of a ring are proportional to its size. However, impulse and energy also depend on the geometry of the vortex ring itself. One key parameter of the ring geometry is the ratio between minor and major axis diameters ( $d/D$ ). When  $d/D$  approaches one, the ring becomes more axisymmetric, which is favorable because axisymmetric rings possess the maximum amount of energy relative to other shapes that maintain the same total impulse (70, 71). Given that  $d$  is always constrained by the span of the tail (7, 58, 59, 62, 72), the axisymmetry of the ring primarily depends on  $D$ . Our results show that during steady swimming trout generate elliptical rings ( $d/D = 0.66$ ). In contrast, we found that during acceleration the geometry of the vortex rings become more axisymmetric ( $d/D = 0.88$ ).

The impulse of a vortex ring is also proportional to the ratio of its core diameter to its ring diameter ( $D_o/D$ ). In addition to having a more axisymmetric shape, we found that the vortex rings generated by accelerating trout have thicker cores ( $D_o/D = 0.37 \pm 0.02$ ) than those generated by trout swimming steadily ( $D_o/D = 0.25 \pm 0.01$ ). It has been shown that for vortex rings generated by a piston pushing a cylinder of fluid through a nozzle there is a limit in generating thicker arms efficiently, because at some point (piston stroke to diameter ratio  $>3.5$ ) separation occurs and energy is dissipated by a trailing edge of fluid (73–75). For finite-core, axisymmetric vortex rings which propagate steadily (76), this piston stroke to diameter ratio corresponds to  $D_o/D = 0.42$  in a vortex ring (77, 78). Perhaps not coincidentally, the vortex rings generated by accelerating trout have  $D_o/D$  close to 0.42. To evaluate whether our fish-generated vortex rings during acceleration can be compared with nozzle-generated rings, we analyzed their velocity and vorticity distributions along a center line connecting the two vortex cores and confirmed that they closely match the values reported for nozzle-generated rings (73, 79) (Fig. S6 A–C). In addition, we investigated the temporal dynamics of vortex rings once they are shed into the wake and found that they translate downstream with a constant velocity while preserving their  $D_o/D$  ratio (Fig. S6D). What this suggests is that the hydrodynamic principles of efficient thrust production in oscillating fish may be similar to those observed during biological jet propulsion (65, 80–82).

Overall, our findings indicate that accelerating trout generate more thrust, not by generating larger rings, but by modulating their geometry and orientation. To investigate how common this phenomenon is, we analyzed  $d/D$ ,  $D_o/D$ , and  $\theta$  of four additional species with different swimming modes and body shapes and found similar results (Table S4). In addition, flow imaging on a similar-sized American eel ( $L = 23$  cm) shows that during acceleration anguilliform swimmers also generate vortex rings with comparable  $D_o/D$  ratio ( $\sim 0.4$  based on figure 1B in ref. 44). It remains to be seen, however, how  $D_o/D$  ratio scales with body size, given that it is significantly higher (0.6–0.7) for smaller fish such as zebrafish (83) and carp (45). Note that a two-dimensional geometric analysis of vortex rings provides an initial, albeit qualitative understanding on how fishes accelerate efficiently.

Concatenated, ring-like structures involved in the wakes of fishes can be highly elongated and three dimensional and may not have the same properties (e.g., momentum, energy, and stability) as nozzle-generated rings.

#### Relationship Between Tail Kinematics and Vortex Ring Geometry.

We next propose a set of equations to provide a mechanistic understanding of how the geometry ( $d/D$  and  $D_o/D$ ) and angle ( $\theta$ ) of a vortex ring depend on the tail kinematics. Because the oscillating tail generates each core of a vortex ring successively, we used trigonometric relations to define  $D = \sqrt{a^2 + b^2}$  and  $\theta = \tan^{-1}(a/b)$ , where  $a$  and  $b$  are the vertical and horizontal spacing between the two cores, respectively. Based on our wake analysis, the vertical spacing depends on the tail-beat amplitude (i.e.,  $a =$  half of the tail-beat amplitude), and the horizontal spacing depends on the tail-beat frequency and swimming speed (i.e.,  $b =$  swimming speed multiplied by half tail-beat cycle). To validate our approach, we calculated  $D$  and  $\theta$  for trout swimming steadily at  $3 L \cdot s^{-1}$  and accelerating from the same initial speed. During acceleration we assumed that the swimming speed was  $4 L \cdot s^{-1}$  (i.e., the average between initial and final swimming speeds). We compared the predicted  $D$  and  $\theta$  to those measured experimentally and found a good match (Fig. 2D,  $D = 0.31 L$  and  $\theta = 75.07^\circ$  during steady swimming and  $D = 0.22 L$  and  $\theta = 63.43^\circ$  during acceleration).

Once we validated our approach, we used it to further investigate the contribution of increased tail-beat amplitude during acceleration. We computationally explored an alternative scenario where the tail-beat amplitude was kept constant at the value observed for steady swimming ( $0.16 L$ ), and speed was gained by further increasing the tail-beat frequency (i.e., hypothetical acceleration). Given that thrust is proportional to the square of tail-beat frequency multiplied by the square of tail-beat amplitude (84, 85), we increased the tail-beat frequency from 10 Hz to 12.5 Hz to maintain the same effective thrust. We found that this had no effect on the ring angle ( $\theta = 63.43^\circ$ ), but generated a suboptimal  $D = 0.18 L$  with  $d/D = 1.22$  and  $D_o/D = 0.56$  (we assumed that  $d = 0.22 L$  and  $D_o = 0.1 L$ ). Therefore, we

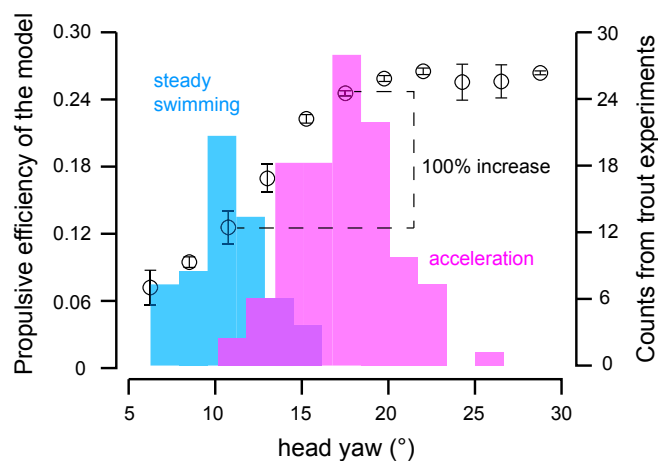


Fig. 3. Fishes adopt acceleration kinematics tuned for high propulsive efficiency. Propulsive efficiency of the physical model as a function of head yaw at flow speed  $1.2 L \cdot s^{-1}$  (left axis, black symbols; error bars are  $\pm 1$  SE); propulsive efficiency increases with increasing head yaw. A histogram of head yaw (right axis) is shown for live trout during steady swimming (blue) and acceleration (magenta). Note that the overlapped region between the distributions of steady swimming and acceleration appears darker. The average head yaw for steady swimming and acceleration is  $12.469 \pm 0.370^\circ$  and  $17.805 \pm 0.352^\circ$ , respectively (unpaired  $t$  test,  $P < 0.01$ ).

believe that the increase in tail-beat amplitude observed in trout is the key to geometrically generating the most efficient rings.

**The Swimming Performance of Robotic Models Increases with Tail-Beat Amplitude.** While it is favorable to generate more thrust by producing vortex rings with optimal geometry, this does not reveal the overall swimming efficiency of an accelerating fish because motions that produce them may be costly. It is not unreasonable to imagine that large lateral body amplitudes would incur large drag penalties (44, 45). To resolve this tradeoff, we employed experiments with a biomimetic trout model to systematically explore how different tail-beat amplitudes affect steady swimming and acceleration performance (Fig. S7). This level of experimental control is impossible to achieve with live fish. We generated undulatory movements in our flexible fish model from a single actuation point located just posterior to the head. Therefore, we were able to control tail-beat amplitude by modulating the head yaw.

We first measured performance during steady swimming and acceleration at yaw amplitudes very similar to those of live fish (10° and 20°). We found that during steady swimming the model performed better when it is actuated with smaller yaw (Fig. S8A). However, during acceleration this relationship is reversed; swimming performance is consistently higher with larger yaw (Fig. S8B). This suggests that there is no convergence of optimum head yaw between steady swimming and acceleration. While steady swimming seeks to preserve momentum by streamlining motions, during acceleration additional momentum must be generated despite drag costs.

To determine whether there are yaw values that maximize swimming efficiency during acceleration, we measured efficiency at yaw amplitudes between 0° and 30° at 3° increments. We found that efficiency increases linearly with yaw amplitudes up to 20°, beyond which values plateau (Fig. 3). When we mapped head yaw from live fish onto our model performance curve, we found that increasing head yaw from steady swimming values to acceleration values can create an increase in efficiency up to 100%. It is perhaps no accident that the yaw amplitudes chosen by accelerating fish fall within the range that gives greatly increased propulsive efficiency compared with steady swimming. We hypothesize that this is due to generating hydrodynamically more efficient vortex rings, based on our flow measurements in the wake of live fishes. However, increasing head yaw to accelerate with more optimal vortex rings does not mean that producing these rings costs less than the rings produced during steady swimming (Fig. S9 shows a 50% increase in mechanical power input for increased head yaw).

The ability to move is one of the key evolutionary events that led to the diversity and complexity of vertebrate life. Given that movement through fluids is energetically costly, fishes have found many ways to minimize drag during normal, steady swimming, such

as keeping the body straight and using median or paired fin locomotion (86–88). While steady swimming is optimized for endurance by minimizing the energetic investment, acceleration favors maximizing force production to escape quickly from predators or capture elusive prey. Here, we show that the enormous behavioral diversity observed during steady swimming collapses into a single locomotion strategy when fishes transition to forward acceleration. We believe that this strategy is likely conserved across all undulatory swimmers and not just fishes because it is hydrodynamically the optimal solution to maximize propulsive efficiency.

## Methods

All research protocols were approved by the Institutional Animal Care and Use Committee at the University of Florida. All data analyses were performed in MATLAB (MathWorks) and all values are shown as mean  $\pm$  SEM, unless stated otherwise.

**Diversity of Swimming Kinematics Across Species.** Our dataset included 51 species of salt- and freshwater fish (105 individuals, from 20 taxonomic orders), which were either obtained from commercial dealers or wild caught using cast net or hook and line. The details about these species are given in Table S1, and the research protocols are described in [Diversity of Swimming Kinematics Across Species \(Extended\)](#).

**Swimming Hydrodynamics of Rainbow Trout.** We used digital particle image velocimetry to quantify the flow fields around and behind steady swimming and accelerating trout. We estimated wake forces as described in ref. 66 [see [Digital Particle Image Velocimetry \(Extended\)](#) for more details on the experimental procedures and data analysis].

**Experiments with the Physical Fish Model.** We performed the experiments in the flow tank at Harvard University, which is customized to house a computer-controlled external actuator. We used this system in the past to evaluate the swimming performance in a number of swimming mechanical models (5, 89–91). Here, we systematically moved the physical model with different tail kinematics and measured the total sum of forces acting on the whole body. For these measurements, we calculated the propulsive force produced by the model and the corresponding power output of the actuator as described in ref. 92 [see [Experiments with the Physical Fish Model \(Extended\)](#) for more details].

**ACKNOWLEDGMENTS.** We thank Sefki Kolozali for his comments on the earlier version of the manuscript. We thank Mikhaila Marecki and Elias Lunsford for helping to conduct fish experiments and digitize fish midlines. We also thank Ashley N. Peterson and Patrick J. M. Thornycroft for helping to design and fabricate fish models and conduct experiments with them. Wild-caught species were collected with the generous assistance of Craig Barzso, Jessica Long, Adam Pacetti, and John Perkner. This work was supported by Office of Naval Research Grant N00014-0910352 (to G.V.L.), Research Coordination Network Grant DBI-RCN 1062052 (to O.A. and J.C.L.), and National Institute on Deafness and Other Communication Disorders Grant R01-DC-010809 and National Science Foundation Grant IOS 1257150 (to J.C.L.).

- Alexander RM (2003) *Principles of Animal Locomotion* (Princeton Univ Press, Princeton).
- Biewener AA (2003) *Animal Locomotion* (Oxford Univ Press, New York).
- Nudds RL, Taylor GK, Thomas ALR (2004) Tuning of Strouhal number for high propulsive efficiency accurately predicts how wingbeat frequency and stroke amplitude relate and scale with size and flight speed in birds. *Proc Biol Sci* 271:2071–2076.
- Gray J (1953) The locomotion of fishes. *Essays in Marine Biology*, eds Marshall SM, Orr AP (Oliver and Boyd, Edinburgh), pp 1–16.
- Akanyeti O, et al. (2016) Fish optimize sensing and respiration during undulatory swimming. *Nat Commun* 7:11044.
- Gemmell BJ, Colin SP, Costello JH, Dabiri JO (2015) Suction-based propulsion as a basis for efficient animal swimming. *Nat Commun* 6:8790.
- Kern S, Koumoutsakos P (2006) Simulations of optimized anguilliform swimming. *J Exp Biol* 209:4841–4857.
- Müller UK, Smit J, Stamhuis EJ, Videler JJ (2001) How the body contributes to the wake in undulatory fish swimming: Flow fields of a swimming eel (*Anguilla anguilla*). *J Exp Biol* 204:2751–2762.
- Nauen JC, Lauder GV (2001) Three-dimensional analysis of finlet kinematics in the chub mackerel (*Scomber japonicus*). *Biol Bull* 200:9–19.
- Borazjani I, Sotiropoulos F (2009) Numerical investigation of the hydrodynamics of anguilliform swimming in the transitional and inertial flow regimes. *J Exp Biol* 212: 576–592.
- Bainbridge R (1958) The speed of swimming of fish as related to size and to the frequency and amplitude of the tail beat. *J Exp Biol* 35:109–133.
- Videler JJ, Hess F (1984) Fast continuous swimming of two pelagic predators, saithe (*Pollachius virens*) and mackerel (*Scomber scombrus*): A kinematic analysis. *J Exp Biol* 109:209–228.
- Webb PW, Kostecki PT, Stevens ED (1984) The effect of size and swimming speed on the locomotor kinematics of rainbow trout. *J Exp Biol* 109:77–95.
- Lauder B (1995) Speed effects on midline kinematics during steady undulatory swimming of largemouth bass, *Micropterus salmoides*. *J Exp Biol* 198:585–602.
- Rome LC, Swank D, Corda D (1993) How fish power swimming. *Science* 261:340–343.
- Jayne BC, Lauder GV (1996) New data on axial locomotion in fishes: How speed affects diversity of kinematics and motor patterns. *Am Zool* 36:642–655.
- Altringham JD, Ellerby DJ (1999) Fish swimming: Patterns in muscle function. *J Exp Biol* 202:3397–3403.
- Coughlin DJ (2002) Aerobic muscle function during steady swimming in fish. *Fish Fish* 3:63–78.
- Videler JJ, Müller UK, Stamhuis EJ (1999) Aquatic vertebrate locomotion: Wakes from body waves. *J Exp Biol* 202:3423–3430.
- Drucker EG, Lauder GV (2002) Experimental hydrodynamics of fish locomotion: Functional insights from wake visualization. *Integr Comp Biol* 42:243–257.
- Lauder GV, Tytell ED (2005) Hydrodynamics of undulatory propulsion. *Fish Physiology*, eds Shadwick R, Lauder GV (Academic, San Diego), Vol 23, pp 425–468.

22. Bainbridge R (1963) Caudal fin and body movements in the propulsion of some fish. *J Exp Biol* 40:23–56.
23. Fish FE (1984) Kinematics of undulatory swimming in the American alligator. *Copeia* 1984:839–843.
24. Fish FE (1998) Comparative kinematics and hydrodynamics of odontocete cetaceans: Morphological and ecological correlates with swimming performance. *J Exp Biol* 201:2867–2877.
25. Kojaszewski T, Fish FE (2007) Swimming kinematics of the Florida manatee (*Trichechus manatus latirostris*): Hydrodynamic analysis of an undulatory mammalian swimmer. *J Exp Biol* 210:2411–2418.
26. Eloy C (2013) On the best design for undulatory swimming. *J Fluid Mech* 717:48–89.
27. Schultz WW, Webb PW (2002) Power requirements of swimming: Do new methods resolve old questions? *Integr Comp Biol* 42:1018–1025.
28. van Rees WM, Gazzola M, Koumoutsakos P (2015) Optimal morphokinematics for undulatory swimmers at intermediate Reynolds numbers. *J Fluid Mech* 775:178–188.
29. Tytell ED, Hsu C-Y, Williams TL, Cohen AH, Fauci LJ (2010) Interactions between internal forces, body stiffness, and fluid environment in a neuromechanical model of lamprey swimming. *Proc Natl Acad Sci USA* 107:19832–19837.
30. Anderson JM, Streitlien K, Barrett DS, Triantafyllou MS (1998) Oscillating foils of high propulsive efficiency. *J Fluid Mech* 360:41–72.
31. Taylor GK, Nudds RL, Thomas AL (2003) Flying and swimming animals cruise at a Strouhal number tuned for high power efficiency. *Nature* 425:707–711.
32. Weihs D, Webb PW (1983) Optimization of locomotion. *Fish Biomechanics*, eds Webb PW, Weihs D (Praeger, New York).
33. Gleiss AC, et al. (2011) Convergent evolution in locomotory patterns of flying and swimming animals. *Nat Commun* 2:352.
34. Rome LC, et al. (1988) Why animals have different muscle fibre types. *Nature* 335:824–827.
35. Johnson TP, Syme DA, Jayne BC, Lauder GV, Bennett AF (1994) Modeling red muscle power output during steady and unsteady swimming in largemouth bass. *Am J Physiol* 267:R481–R488.
36. Weihs D (1974) Energetic advantages of burst swimming of fish. *J Theor Biol* 48:215–229.
37. Videler JJ, Weihs D (1982) Energetic advantages of burst-and-coast swimming of fish at high speeds. *J Exp Biol* 97:169–178.
38. Eaton RC, Bombardieri RA, Meyer DL (1977) The Mauthner-initiated startle response in teleost fish. *J Exp Biol* 66:65–81.
39. Domenici P, Blake R (1997) The kinematics and performance of fish fast-start swimming. *J Exp Biol* 200:1165–1178.
40. Wakeling JM (2006) Fast-start mechanics. *Fish Biomechanics*, eds Shadwick RE, Lauder GV (Academic, San Diego), pp 333–368.
41. Tytell ED, Lauder GV (2008) Hydrodynamics of the escape response in bluegill sunfish, *Lepomis macrochirus*. *J Exp Biol* 211:3359–3369.
42. Fierstine HL, Walters V (1968) Studies in locomotion and anatomy of scombroid fishes. *Mem South California Acad Sci* 6:1–31.
43. Videler JJ (1993) *Fish Swimming* (Chapman and Hall, New York).
44. Tytell ED (2004) Kinematics and hydrodynamics of linear acceleration in eels, *Anguilla rostrata*. *Proc Biol Sci* 271:2535–2540.
45. Wu G, Yang Y, Zeng L (2007) Kinematics, hydrodynamics and energetic advantages of burst-and-coast swimming of koi carps (*Cyprinus carpio koi*). *J Exp Biol* 210:2181–2191.
46. van Leeuwen JL, Lankheet MJM, Akster HJ, Osse JWM (1990) Function of red axial muscles of carp (*Cyprinus carpio* L.): Recruitment and normalized power output during swimming in different modes. *J Zool* 220:123–145.
47. Drucker EG, Lauder GV (2003) Function of pectoral fins in rainbow trout: Behavioral repertoire and hydrodynamic forces. *J Exp Biol* 206:813–826.
48. Drucker EG, Lauder GV (2005) Locomotor function of the dorsal fin in rainbow trout: Kinematic patterns and hydrodynamic forces. *J Exp Biol* 208:4479–4494.
49. Coughlin DJ (2000) Power production during steady swimming in largemouth bass and rainbow trout. *J Exp Biol* 203:617–629.
50. Ellerby DJ, Altringham JD (2001) Spatial variation in fast muscle function of the rainbow trout *Oncorhynchus mykiss* during fast-starts and sprinting. *J Exp Biol* 204:2239–2250.
51. Liao JC, Beal DN, Lauder GV, Triantafyllou MS (2003) The Kármán gait: Novel body kinematics of rainbow trout swimming in a vortex street. *J Exp Biol* 206:1059–1073.
52. Akanyeti O, Liao JC (2013) The effect of flow speed and body size on Kármán gait kinematics in rainbow trout. *J Exp Biol* 216:3442–3449.
53. Stewart WJ, Tian FB, Akanyeti O, Walker CJ, Liao JC (2016) Refuging rainbow trout selectively exploit flows behind tandem cylinders. *J Exp Biol* 219:2182–2191.
54. Akanyeti O, Liao JC (2013) A kinematic model of Kármán gaiting in rainbow trout. *J Exp Biol* 216:4666–4677.
55. Müller UK, Stamhuis EJ, Videler JJ (2000) Hydrodynamics of unsteady fish swimming and the effects of body size: Comparing the flow fields of fish larvae and adults. *J Exp Biol* 203:193–206.
56. Tytell ED, Lauder GV (2004) The hydrodynamics of eel swimming: I. Wake structure. *J Exp Biol* 207:1825–1841.
57. Gemmill BJ, et al. (2016) How the bending kinematics of swimming lampreys build negative pressure fields for suction thrust. *J Exp Biol* 219:3884–3895.
58. Flammang BE, Lauder GV, Troolin DR, Strand TE (2011) Volumetric imaging of fish locomotion. *Biol Lett* 7:695–698.
59. Mendelson L, Techet AH (2015) Quantitative wake analysis of a freely swimming fish using 3D synthetic aperture PIV. *Exp Fluids* 56:135.
60. Tytell ED, Standen EM, Lauder GV (2008) Escaping Flatland: Three-dimensional kinematics and hydrodynamics of median fins in fishes. *J Exp Biol* 211:187–195.
61. Blickhan R, Krick C, Zehren D, Nachtigall W, Breithaupt T (1992) Generation of a vortex chain in the wake of a Subundulatory swimmer. *Naturwissenschaften* 79:220–221.
62. Nauen JC, Lauder GV (2002) Hydrodynamics of caudal fin locomotion by chub mackerel, *Scomber japonicus* (Scombridae). *J Exp Biol* 205:1709–1724.
63. Müller UK, Van den Heuvel BLE, Stamhuis EJ, Videler JJ (1997) Fish foot prints: Morphology and energetics of the wake behind a continuously swimming mullet (*Chelon labrosus* Risso). *J Exp Biol* 200:2893–2906.
64. Drucker EG, Lauder GV (1999) Locomotor forces on a swimming fish: Three-dimensional vortex wake dynamics quantified using digital particle image velocimetry. *J Exp Biol* 202:2393–2412.
65. Bartol IK, Krueger PS, Stewart WJ, Thompson JT (2009) Hydrodynamics of pulsed jetting in juvenile and adult brief squid *Lolliguncula brevis*: Evidence of multiple jet ‘modes’ and their implications for propulsive efficiency. *J Exp Biol* 212:1889–1903.
66. Epps BP, Techet AH (2007) Impulse generated during unsteady maneuvering of swimming fish. *Exp Fluids* 43:691–700.
67. Noca F, Shields D, Jeon D (1999) A comparison of methods for evaluating time-dependent fluid dynamic forces on bodies, using only velocity fields and their derivatives. *J Fluids Struct* 13:551–578.
68. Dabiri JO (2005) On the estimation of swimming and flying forces from wake measurements. *J Exp Biol* 208:3519–3532.
69. Batchelor GK (2000) *An Introduction to Fluid Dynamics* (Cambridge Univ Press, Cambridge, UK).
70. Kelvin L (1880) Vortex statistics. *Philos Mag* 10:97–109.
71. Dabiri JO (2009) Optimal vortex formation as a unifying principle in biological propulsion. *Annu Rev Fluid Mech* 41:17–33.
72. Borazjani I, Daghooghi M (2013) The fish tail motion forms an attached leading edge vortex. *Proc Biol Sci* 280:20122071.
73. Gharib M, Rambod E, Shariff K (1998) A universal time scale for vortex ring formation. *J Fluid Mech* 360:121–140.
74. Krueger PS, Gharib M (2005) Thrust augmentation and vortex ring evolution in a fully pulsed jet. *AIAA J* 43:792–801.
75. Mohseni K, Gharib M (1998) A model for universal time scale of vortex ring formation. *Phys Fluids* 10:2436–2438.
76. Norbury J (1973) Family of steady vortex rings. *J Fluid Mech* 57:417–431.
77. Linden PF, Turner JS (2004) ‘Optimal’ vortex rings and aquatic propulsion mechanisms. *Proc Biol Sci* 271:647–653.
78. Linden PF, Turner JS (2001) The formation of ‘optimal’ vortex rings, and the efficiency of propulsion devices. *J Fluid Mech* 427:61–72.
79. Weigand A, Gharib M (1997) On the evolution of laminar vortex rings. *Exp Fluids* 22:447–457.
80. Dabiri JO, Colin SP, Katija K, Costello JH (2010) A wake-based correlate of swimming performance and foraging behavior in seven co-occurring jellyfish species. *J Exp Biol* 213:1217–1225.
81. Gharib M, Rambod E, Kheradvar A, Sahn DJ, Dabiri JO (2006) Optimal vortex formation as an index of cardiac health. *Proc Natl Acad Sci USA* 103:6305–6308.
82. Dabiri JO, Colin SP, Costello JH (2006) Fast-swimming hydromedusae exploit velar kinematics to form an optimal vortex wake. *J Exp Biol* 209:2025–2033.
83. Müller UK, van Leeuwen JL (2004) Swimming of larval zebrafish: Ontogeny of body waves and implications for locomotory development. *J Exp Biol* 207:853–868.
84. Wu TY (1977) Introduction to scaling of aquatic animal locomotion. *Scale Effects of Animal Locomotion*, ed Pedley TJ (Academic, New York), pp 203–232.
85. Lighthill J (1971) Large-amplitude elongated body theory of fish locomotion. *Proc R Soc Lond B Biol Sci* 179:125–138.
86. Lighthill J (1993) Estimates of pressure differences across the head of a swimming clupeid fish. *Philos Trans R Soc Lond B Biol Sci* 341:129–140.
87. Webb PW (1992) Is the high cost of body/caudal fin undulatory swimming due to increased friction drag or inertial recoil? *J Exp Biol* 162:157–166.
88. Fish FE (1998) Imaginative solutions by marine organisms for drag reduction. Available at darwin.wcupa.edu/faculty/fish/uploads/Main/1998ImaginativeDragReduction.pdf. Accessed November 30, 2017.
89. Lauder GV, Flammang B, Alben S (2012) Passive robotic models of propulsion by the bodies and caudal fins of fish. *Integr Comp Biol* 52:576–587.
90. Shelton RM, Thornycroft PJ, Lauder GV (2014) Undulatory locomotion of flexible foils as biomimetic models for understanding fish propulsion. *J Exp Biol* 217:2110–2120.
91. Lauder GV, Tangorra JL (2015) Fish locomotion: Biology and robotics of body and fin-based movements. *Robot Fish - Bioinspired Fishlike Underwater Robots*, eds Du R, Li Z, Youcef-Toumi K, Alvarado PVY (Springer, Berlin), pp 25–49.
92. Read DA, Hover FS, Triantafyllou MS (2003) Forces on oscillating foils for propulsion and maneuvering. *J Fluids Struct* 17:163–183.



# Supporting Information

Akanyeti et al. 10.1073/pnas.1705968115

## Diversity of Swimming Kinematics Across Species (Extended)

We swam all fishes in recirculating flow tanks at the Whitney Laboratory to measure the tail-beat amplitude and frequency during steady swimming and acceleration. For each species, we recorded at least 10 steady swimming and 10 acceleration movies at 500 frames per second. We were able to elicit self-motivated accelerations for all species by slowly increasing the flow speed from  $1 L \cdot s^{-1}$  up to  $5 L \cdot s^{-1}$ . To determine the effects of body shape, we categorized species into three groups: (i) elongate (e.g., Northern barracuda, *Sphyræna foetens*), (ii) fusiform (e.g., red drum, *Sciaenops ocellatus*), and (iii) laterally compressed (e.g., pinfish, *Lagodon rhomboides*). To determine the effects of swimming mode, we categorized species into seven groups: (i) anguilliform (oyster toadfish, *Opsanus tau*), (ii) carangiform (crevalle jack, *Caranx hippos*), (iii) thunniform (round scad, *Decapterus punctatus*), (iv) labriform (sergeant major, *A. saxatilis*), (v) balistiform (green filefish, *Monacanthus ciliatus*), (vi) gymnotiform (clown knifefish, *Chitala ornata*), and (vii) diodontiform (striped burr fish, *C. schoepfii*). We restricted our swimming mode analysis to anguilliform and carangiform swimmers as the majority of our samples came from these two groups. We determined the relationship between tail-beat amplitude and body length using a power function  $AL^B$ , where coefficients  $A$  and  $B$  indicate initial tail-beat amplitude and decrease rate, respectively. For 10 species, we also analyzed the following parameters: body amplitude envelope, phase difference between head and tail movements, slip ratio, Strouhal number, and the maximum angle of attack of the tail.

To provide more detailed analysis on swimming kinematics, we swam rainbow trout ( $L = 22.4 \pm 2.0$  cm,  $n = 7$  fish) at flow speeds between  $0.5 L \cdot s^{-1}$  and  $5 L \cdot s^{-1}$ . We recorded kinematics of steady swimming and acceleration, using a high-speed camera (Phantom V12) at 500 frames per second. At swimming speeds up to  $5 L \cdot s^{-1}$ , fish swam steadily. For each individual, three trials of steady swimming were conducted at each swimming speed with each trial consisting of an at-least three tail-beat sequence. At swimming speeds greater than  $3 L \cdot s^{-1}$ , trout naturally accelerated upstream in bouts in the flow tank. For each individual, a total of 20 acceleration events were recorded. After extracting body midlines, we first looked at how amplitude envelopes of body movements vary between steady swimming and acceleration. We then measured tail-beat frequency, tail-beat amplitude, and head angle. Tail-beat amplitude and head angle were measured as the distance between maximum right and left excursions. We calculated the phase difference between head and tail movements using a cross-correlation method, with positive values indicating that head movements precede the tail movements.

## Digital Particle Image Velocimetry (Extended)

We seeded the flow with neutrally buoyant, light-reflective particles with an average diameter of  $14 \mu\text{m}$  (Potters Industries), which were illuminated by a horizontal laser sheet ( $25 \text{ cm} \times 15 \text{ cm} \times 0.1 \text{ cm}$ ) parallel to the swimming direction. The laser sheet was generated by a 5-W, continuous argon ion laser with wavelength of  $532 \text{ nm}$  (LaVision). A high-speed camera (Phantom Miro M310) positioned underneath the working section captured images ( $1,280 \times 800$  pixels) of the fish and the particle field at 1,000 frames per second. In addition, to ensure that we captured the precise symmetry plane of the vortex rings relative to the fish we used a second synchronized, lateral view camera. We recorded trials only when the laser plane bisected the span of

the tail and when the fish was swimming horizontally without deviations in pitch angle (with the dorsal–ventral axis of the fish oriented perpendicular to the laser plane). Conveniently, fishes exhibit a robust rheotactic behavior in fast flows in which they orient straight into the flow with minimal deviations in pitch or yaw to minimize drag. Data were collected from the same five individuals used in kinematics experiments, although our data analysis focused on comprehensive datasets from two individuals ( $L = 25 \text{ cm}$  and  $32 \text{ cm}$ ). For each individual, we analyzed 10 steady swimming and 10 acceleration events with each event consisting of at least one tail-beat sequence. Steady swimming events were recorded at swimming speeds between  $1 L \cdot s^{-1}$  and  $3 L \cdot s^{-1}$ , and acceleration events were recorded at an initial swimming speed of  $3 L \cdot s^{-1}$ .

We quantified the flow fields from particle image velocimetry recordings, using commercial software (DaVis; LaVision). Each movie image was divided equally into a  $20 \times 12$  grid of windows that were each  $64 \text{ pixels} \times 64 \text{ pixels}$  in size. Cross-correlation was performed on the corresponding windows of sequential images to determine the average particle displacements between images for all windows in the grid. To improve the spatial resolution of our measurements, we performed a second cross-correlation routine on a finer window grid ( $32 \text{ pixels} \times 32 \text{ pixels}$ ) with a 50% overlap. Data were smoothed and interpolated onto a regular grid using a  $3 \times 3$  spline algorithm. For each dataset, mean background flow was measured and subtracted from all flow fields.

To estimate the impulse, we first selected the flow-field region that contained two counterrotating vortices (i.e., vortex core) which belonged to the same ring. Assuming that the vortex rings are axisymmetric with a finite core, we define impulse ( $I$ ) as

$$I = \rho \Gamma \frac{\pi D^2}{4} \left[ 1 + \frac{3}{4} \frac{D_o^2}{D^2} \right],$$

where  $\rho$  is the fluid density, and  $\Gamma$  is the circulation ( $\Gamma = \iint \omega \, dx' \, dy'$ ),

where  $\omega$  is the vorticity, and  $x'$  and  $y'$  are the two orthogonal axes parallel and perpendicular to the center line of the vortex ring, respectively. We then used jet angle to calculate the proportion of the impulse devoted to forward acceleration ( $I_{\parallel} = I \cos(\theta)$ ). We calculated  $\Gamma$ ,  $\theta$ ,  $D_o$ , and  $D$  as well as the integral area of circulation. We approximated the integral area of circulation by fitting a smallest possible area that enclosed the two vortex cores completely. Here, we assumed that the flow field around the vortex ring has negligible influence on impulse calculations. We calculated the angle between the center line connecting two vortex cores and the axis of swimming to arrive at  $\theta$ , with  $0^\circ$  and  $90^\circ$  indicating parallel and perpendicular to the axis of swimming, respectively. We identified each vortex core as a connected region with vorticity higher than 25% of maximum vorticity. We estimated  $D_o$  by fitting a smallest possible circle that enclosed the vortex core completely. We estimated  $D$  as the distance between the centers two vortex cores. To minimize measurement noise, we averaged values calculated for three consecutive frames immediately after a vortex ring is formed. Note that our method overestimates the impulse of trout swimming steadily as their vortex rings are elliptical. Therefore, the relative increase in impulse when fish transition from steady swimming to acceleration can be higher than that reported in this study. We also analyzed the geometry of the vortex rings, using two parameters: (i)  $D_o/D$  describes the relative core thickness of the vortex

ring, with 0 and 1 corresponding to minimum and maximum values, respectively, and (ii)  $d/D$  describes the overall shape of the ring, with 1 corresponding to an axisymmetric vortex ring.

### Experiments with the Physical Fish Model (Extended)

We designed the physical model based on the scanned images of rainbow trout. The model consisted of a rigid head, a flexible (but not articulated) backbone, and a soft body. The backbone included a vertebral column and median fins (caudal, anal, and dorsal). The head, backbone, and fish mold were 3D printed. We placed the printed head and the backbone into the mold and injected liquid plastisol to make the soft body. The physical model had a mounting rod (8-mm diameter stainless steel) located just posterior to the head and was connected to a computer-controlled actuator. The actuator had 2 df, which allowed us to independently and simultaneously heave and yaw the model at a fixed point. A customized script (LabVIEW; National Instruments) was used to actuate the model and record the experimental data. We actuated the model using sine waves for both heave ( $h$ ) and yaw ( $\theta$ ) movements,

$$h(t) = A_h \sin(2\pi ft)$$

$$\theta(t) = A_\theta \sin(2\pi ft + \varphi),$$

where  $t$  is the time stamp. We kept the amplitude of heave constant at  $A_h = 1$  cm. We swam the model over a range of flow speeds ( $0.2$ – $2.0$   $L \cdot s^{-1}$  in  $0.2$   $L \cdot s^{-1}$  increments) and varied yaw amplitude ( $A_\theta = 0^\circ$ – $30^\circ$  in  $3^\circ$  increments), oscillation frequency ( $f = 0.5$ – $2.5$  Hz in  $0.25$ -Hz increments), and phase difference between heave and yaw movements ( $\varphi = 0^\circ$ – $360^\circ$  in  $30^\circ$  increments). For all experiments, we recorded the forces and torques on the mounting rod, using a six-axis force/torque transducer (ATI-Nano 17) for 10 tail beats, and smoothed the measured data using a 10-Hz low-pass filter.

We evaluated the performance of the model during steady swimming and acceleration. Fishes swimming steadily move at a constant velocity, with no net force acting on the body. Therefore, to emulate steady-swimming conditions, we exposed the model to a constant background flow and identified combinations of tail-beat amplitude and frequency that would produce enough thrust to counter the fluid drag forces, ensuring that the net force acting on the model is zero (i.e., thrust is equal to drag). To evaluate the swimming performance for each combination of tail-beat amplitude and frequency, we measured the mechanical power invested in the model to satisfy this condition and normalized it by the swimming velocity [i.e., cost of transport (COT)], where a low COT indicates a high swimming performance. In contrast, to emulate acceleration conditions, we identified combinations of tail-beat amplitude and frequency that would produce a net force in the direction of swimming (thrust > drag). Because of this surplus of net force, we evaluated swimming performance in terms of propulsive efficiency (net force multiplied by speed divided by power). For each flow speed and yaw amplitude, we identified the combination of actuation parameters (oscillation frequency and phase difference) that led to minimum COT and maximum propulsive efficiency. We then analyzed how swimming performance changed as a function of yaw amplitude to identify optimum swimming strategy for both steady swimming and acceleration.

To account for the fluid resistance of the rod, we repeated the experiments only with the rod (no model), and these values were subtracted from the original experiments. For a subset of experiments, we recorded swimming kinematics of the model, using a high-speed camera (Photron PCI-1024) at a sampling frequency of 250 Hz so that we could provide a more detailed analysis of the effect of a combination of the actuation parameters. For each experiment, two trials were conducted with each trial consisting of a 10-tail-beat sequence. Procedures for extraction of the midlines and kinematics analysis were identical to those for live fish.

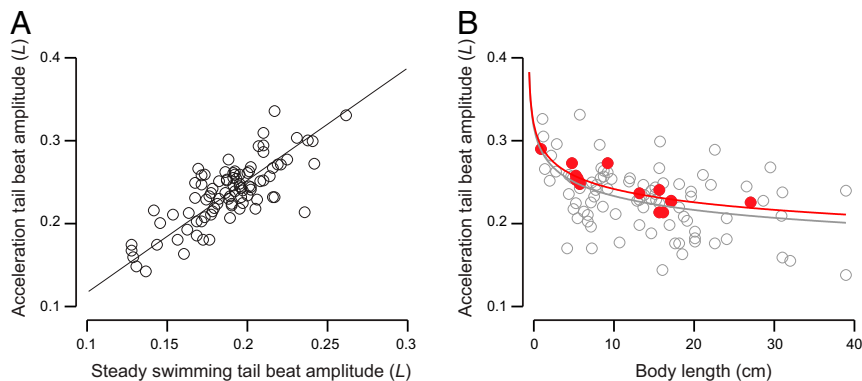


**Fig. 51.** (A) Tail-beat amplitude during acceleration vs. during steady swimming ( $y = 1.34x$ ,  $R^2 = 0.62$ ,  $P < 0.001$ , all species are included in the analysis). (B) Tail-beat amplitude during acceleration decreases with body length (i) in pinfish (red,  $0.33 L^{-0.1}$ ,  $R^2 = 0.73$ ) and (ii) when all 51 species (Table S1) are included in the analysis (gray,  $0.32 L^{-0.1}$ ,  $R^2 = 0.25$ , Kolmogorov–Smirnov test,  $P < 0.001$ ). The relationship between the tail-beat amplitude and body length is valid only for the range of body lengths tested in this study (i.e., 1–40 cm). Further experiments are needed to reevaluate this relationship for more extreme body sizes.







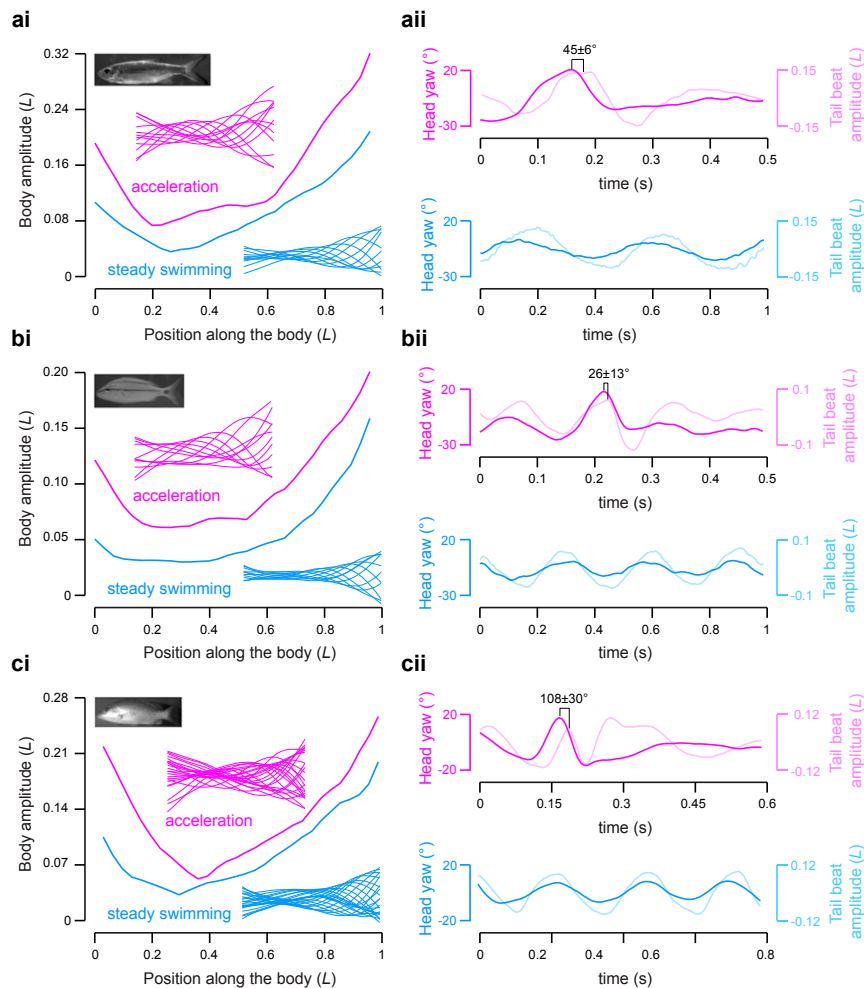


**Fig. S4.** Midline kinematics of fusiform fishes during steady swimming and acceleration. (A, *i*) Amplitude envelope of an Indo-Pacific tarpon ( $L = 23$  cm) swimming steadily at  $2.7 L \cdot s^{-1}$  (blue) and accelerating from an initial speed of  $3.7 L \cdot s^{-1}$  (magenta). Representative midlines for one tail-beat cycle are also shown. (A, *ii*) Head yaw and tail-beat amplitude and head yaw of the same fish vs. time for the same trial. The phase difference between head yaw and tail-beat amplitude during acceleration is shown where error represents a value dictated by our sampling frequency. (B, *i*) Amplitude envelope of a tomtate ( $L = 20$  cm) swimming steadily at  $2.6 L \cdot s^{-1}$  (blue) and accelerating from an initial speed of  $4.7 L \cdot s^{-1}$  (magenta). Representative midlines for one tail-beat cycle are also shown. (B, *ii*) Head yaw and tail-beat amplitude of the same fish vs. time for the same trial. The phase difference between head yaw and tail-beat amplitude during acceleration is shown where error represents a value dictated by our sampling frequency. (C, *i*) Amplitude envelope of a mangrove snapper ( $L = 23$  cm) swimming steadily at  $3.2 L \cdot s^{-1}$  (blue) and accelerating from the same initial speed (magenta). Representative midlines for one tail-beat cycle are also shown. (C, *ii*) Head yaw and tail-beat amplitude of the same fish vs. time for the same trial. The phase difference between head yaw and tail-beat amplitude during acceleration is shown where error represents a value dictated by our sampling frequency.











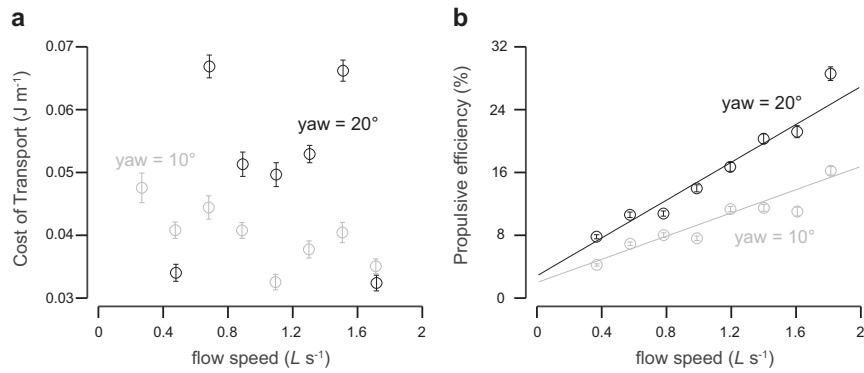


**Fig. 58.** Swimming performance of the physical fish model during steady swimming and acceleration. (A) Cost of transport of steady swimming as a function of flow speed when the model was actuated at yaw amplitudes of 10° (gray) and 20° (black). At intermediate speeds (0.5–1.5 L s<sup>-1</sup>), the model had significantly lower cost of transport (i.e., higher power efficiency) when it was actuated with the lower yaw amplitude. (B) In contrast, the propulsive efficiency of the accelerating model was consistently higher when it was actuated with the higher yaw amplitude. At 20°, propulsive efficiency increased linearly with flow speed ( $y = 0.11x - 0.04$ ,  $R^2 = 0.92$ ,  $P < 0.01$ ), with a slope significantly higher than that of 10° ( $y = 0.07x + 0.03$ ,  $R^2 = 0.90$ ,  $P < 0.01$ ). Error bars are  $\pm 1$  SE.

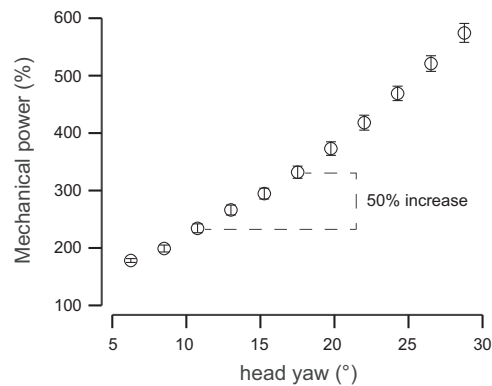


**Fig. 59.** Mechanical power of the physical model as a function of head yaw at the same flow speed (black symbols; error bars are  $\pm 1$  SE). Values are normalized to the power value measured for steady swimming (0.01 N·m·s<sup>-1</sup>).

**Table S1. List of all fish species tested in this study, along with the corresponding total body length, body shape, and swimming mode**

| Common name                 | Species name                        | No. of fish | Length, cm | Body shape | Swimming mode |
|-----------------------------|-------------------------------------|-------------|------------|------------|---------------|
| Atlantic menhaden           | <i>Brevoortia tyrannus</i>          | 4           | 8.5–10     | F          | C             |
| Bala shark                  | <i>Belantiocheilos melanopterus</i> | 2           | 6.0–6.2    | F          | C             |
| Bamboo shark                | <i>Chiloscyllium plagiosum</i>      | 3           | 21.0       | E          | A             |
| Black molly                 | <i>Poecilia latipinnis</i>          | 2           | 5.1–5.4    | F          | C             |
| Black seabass               | <i>Centropristis striata</i>        | 1           | 40.0       | F          | M             |
| Bluefish                    | <i>Pomatomus saltatrix</i>          | 1           | 25.0       | F          | C             |
| Bluegill sunfish            | <i>Lepomis macrochirus</i>          | 2           | 17.8–19.6  | D          | C             |
| Bonnethead shark            | <i>Sphyrna tiburo</i>               | 1           | 38.0       | E          | A             |
| Bumblebee cichlid           | <i>Pseudotropheus crabro</i>        | 1           | 5.7        | D          | C             |
| Chinese hi-fin banded shark | <i>Myxocyprinus asiaticus</i>       | 1           | 21.9       | F          | C             |
| Clown knifefish             | <i>Chitala ornata</i>               | 1           | 19.4       | D          | M             |
| Crevalle jack               | <i>Caranx hippos</i>                | 1           | 20.5       | D          | C             |
| Dojo loach                  | <i>Misgurnus anguillicaudatus</i>   | 2           | 9.2        | E          | A             |
| Emerald goby                | <i>Ctenogobius smaragdus</i>        | 1           | 8.6        | E          | C             |
| Florida gar                 | <i>Lepisosteus platyrhincus</i>     | 1           | 36.9       | E          | C             |
| Freshwater angelfish        | <i>Pterophyllum scalare</i>         | 1           | 7.0        | D          | C             |
| Goldfish                    | <i>Carassius auratus</i>            | 2           | 5.1–5.6    | D          | C             |
| Green filefish              | <i>Monacanthus ciliatus</i>         | 2           | 2.1–2.7    | D          | M             |
| Hairy blenny                | <i>Labrisomus nuchipinnis</i>       | 1           | 16.0       | E          | C             |
| Indonesian datnoid          | <i>Datnioides microlepis</i>        | 1           | 12.2       | D          | C             |
| Indo-Pacific tarpon         | <i>Megalops cyprinoides</i>         | 5           | 12.7–16.6  | D          | C             |
| Inshore lizardfish          | <i>Synodus foetens</i>              | 1           | 31.9       | E          | C             |
| Iridescent shark            | <i>Pangasianodon hypophthalmus</i>  | 1           | 6.5        | E          | C             |
| Mangrove snapper            | <i>Lutjanus griseus</i>             | 2           | 10.0–23.0  | D          | C             |
| Mojarra                     | <i>Eucinostomus</i> sp.             | 4           | 1.8–9.4    | D          | C             |
| Mummichog                   | <i>Fundulus heteroclitus</i>        | 2           | 7.5–11.0   | F          | C             |
| Needlefish                  | <i>Belonidae</i>                    | 1           | 1.9        | E          | A             |
| Northern barracuda          | <i>Sphyrna borealis</i>             | 1           | 33.0       | E          | C             |
| Oyster toadfish             | <i>Opsanus tau</i>                  | 2           | 9.0–30.5   | F          | A             |
| Pinfish                     | <i>Lagodon rhomboides</i>           | 15          | 1.6–18.0   | D          | C             |
| Pipefish                    | Syngnathidae                        | 1           | 8.0        | E          | M             |
| Purplemouth moray           | <i>Gymnothorax vicinus</i>          | 1           | 40.0       | E          | A             |
| Rainbow trout               | <i>Oncorhynchus mykiss</i>          | 7           | 15.5–32.0  | F          | C             |
| Red drum                    | <i>Sciaenops ocellatus</i>          | 1           | 29.6       | F          | C             |
| Round scad                  | <i>Decapterus punctatus</i>         | 4           | 14.0–16.5  | F          | C             |
| Royal pleco                 | <i>Panaque nigrolineatus</i>        | 1           | 9.5        | F          | A             |
| Saddled bichir              | <i>Polypterus endlicheri</i>        | 1           | 7.9        | E          | A             |
| Scrawled filefish           | <i>Aluterus scriptus</i>            | 1           | 4.9        | D          | M             |
| Sergeant major              | <i>Abudefduf saxatilis</i>          | 1           | 11.5       | D          | C             |
| Sharksucker                 | <i>Echeneis naucrates</i>           | 1           | 13.7       | E          | A             |
| Sheepshead                  | <i>Archosargus probatocephalus</i>  | 1           | 32.0       | D          | C             |
| Southern kingfish           | <i>Menticirrhus americanus</i>      | 2           | 22.0–23.5  | F          | C             |
| Spadefish                   | <i>Chaetodipterus faber</i>         | 2           | 10.5–27.5  | D          | C             |
| Spanish sardine             | <i>Sardinella aurita</i>            | 4           | 15.5–19.0  | F          | C             |
| Spot                        | <i>Leiostomus xanthurus</i>         | 2           | 7.5–20.5   | F          | C             |
| Striped burrfish            | <i>Chilomycterus schoepfii</i>      | 1           | 14.0       | F          | M             |
| Striped mullet              | <i>Mugil cephalus</i>               | 3           | 2.9–16.5   | F          | C             |
| Summer flounder             | <i>Paralichthys dentatus</i>        | 1           | 9.1        | D          | C             |
| Tinfoil barb                | <i>Barbonymus schwanenfeldii</i>    | 2           | 6.5–8.0    | D          | C             |
| Tomtate                     | <i>Haemulon aurolineatum</i>        | 2           | 19.0–20.0  | F          | C             |
| Zebrafish                   | <i>Danio rerio</i>                  | 2           | 3.5–3.6    | F          | C             |

A, anguilliform; C, carangiform; D, laterally compressed; E, elongate; F, fusiform; M, median and paired fin swimming.

**Table S2. Analyses of kinematic parameters which relate to efficient force production during swimming**

| Fish species        | Slip ratio  | St          | $\alpha_{max}$ , ° |
|---------------------|-------------|-------------|--------------------|
| Crevalle jack       | 0.51 ± 0.01 | 0.51 ± 0.01 | 29.3 ± 0.4         |
| Pinfish             | 1.03 ± 0.17 | 0.39 ± 0.06 | 24.1 ± 2.4         |
| Sheepshead          | 0.55 ± 0.07 | 0.38 ± 0.05 | 24.5 ± 3.6         |
| Florida gar         | 1.05 ± 0.05 | 0.35 ± 0.02 | 15.2 ± 2.4         |
| Northern barracuda  | 0.75 ± 0.06 | 0.42 ± 0.05 | 34.1 ± 2.4         |
| Clown knifefish     | 0.83 ± 0.03 | 0.37 ± 0.03 | 23.5 ± 1.8         |
| Indo-Pacific tarpon | 0.89 ± 0.02 | 0.48 ± 0.01 | 11.4 ± 0.7         |
| Tomtate             | 0.91 ± 0.05 | 0.42 ± 0.02 | 24.8 ± 1.4         |
| Mangrove snapper    | 0.76 ± 0.05 | 0.48 ± 0.06 | 20.9 ± 2.4         |
| Rainbow trout       | 0.71 ± 0.02 | 0.32 ± 0.01 | 19.3 ± 0.7         |

Values are shown for the datasets from 10 species presented in Figs. S2–S5 (i.e., one acceleration trial per fish and error represents a measurement uncertainty dictated by our sampling frequency).  $\alpha_{max}$ , maximum angle of attack; slip ratio, swimming speed divided by body wave speed; St, Strouhal number.

**Table S3. Regression analyses to evaluate how acceleration and steady swimming speed depend on tail-beat amplitude and frequency**

| Tail kinematics                         | N  | Multiple linear regression |      |        |                | Linear regression |        |                |
|---|----|----------------------------|------|--------|----------------|-------------------|--------|----------------|
|   |    | Coefficients               | t    | P      | R <sup>2</sup> | Coefficients      | P      | R <sup>2</sup> |
| Maximum acceleration, $L \cdot s^{-2}$  | 93 |                            |      |        | 0.62           |                   |        |                |
| Tail-beat amplitude, L                  |    | 51.93 ± 17.82              | 2.9  | 0.005  |                | 86.2 ± 53.38      | 0.002  | 0.10           |
| Tail-beat frequency, Hz                 |    | 1.15 ± 0.10                | 11.1 | <0.001 |                | 1.21 ± 0.21       | <0.001 | 0.59           |
| Steady swimming speed, $L \cdot s^{-1}$ | 49 |                            |      |        | 0.91           |                   |        |                |
| Tail-beat frequency                     |    | 0.67 ± 0.03                | 21.3 | <0.001 |                | 0.67 ± 0.06       | <0.001 | 0.91           |

Multiple-regression analysis suggests that acceleration increases with both tail-beat amplitude and tail-beat frequency. However, the contribution of tail-beat amplitude on predicting acceleration is significantly lower than the contribution of tail-beat frequency (linear-regression analysis). Steady swimming speed does not depend on the tail amplitude. Only statistically significant relationships are shown. N indicates the number of events analyzed for acceleration and steady swimming. t, t test.

**Table S4. Vortex ring geometry and orientation behind (i) clown knifefish ( $L = 24$  cm) swimming steadily at  $1.5 L \cdot s^{-1}$  and accelerating from the same initial speed, (ii) crevalle jack ( $L = 45.5$  cm) swimming steadily at  $1.3 L \cdot s^{-1}$  and accelerating from  $3.1 L \cdot s^{-1}$ , (iii) Florida gar ( $L = 36.9$  cm) swimming steadily at  $0.8 L \cdot s^{-1}$  and accelerating from  $1.0 L \cdot s^{-1}$ , and (iv) Indo-Pacific tarpon ( $L = 20.2$  cm) swimming steadily at  $2.5 L \cdot s^{-1}$  and accelerating from  $5 L \cdot s^{-1}$** 

| Fish species        | Steady swimming |             |              | Forward acceleration |             |              |
|---------------------|-----------------|-------------|--------------|----------------------|-------------|--------------|
|                     | d/D             | $D_o/D$     | $\theta$ , ° | d/D                  | $D_o/D$     | $\theta$ , ° |
| Clown knifefish     | 0.58 ± 0.00     | 0.27 ± 0.02 | 76.38 ± 0.44 | 0.95 ± 0.01          | 0.43 ± 0.00 | 67.95 ± 0.51 |
| Crevalle jack       | 0.75 ± 0.01     | 0.21 ± 0.01 | 75.92 ± 0.27 | 1.03 ± 0.01          | 0.30 ± 0.02 | 63.28 ± 0.28 |
| Florida gar         | 0.46 ± 0.00     | 0.25 ± 0.01 | 83.64 ± 0.24 | 0.60 ± 0.00          | 0.37 ± 0.01 | 47.16 ± 0.35 |
| Indo-Pacific tarpon | 1.18 ± 0.01     | 0.33 ± 0.01 | 85.73 ± 0.72 | 1.09 ± 0.01          | 0.38 ± 0.01 | 53.08 ± 0.62 |

The values of d/D,  $D_o/D$ , and  $\theta$  are shown as mean ± SEM, and they are statistically different between steady swimming and acceleration (unpaired t test,  $P < 0.01$ ).